aerospace

MDPI

Article

Analysis and Control for the Mode Transition of Tandem-Wing Aircraft with Variable Sweep

Liang Gao, Yanhe Zhu, Yubin Liu *, Junming Zhang, Benshan Liu and Jie Zhao *

State Key Laboratory of Robotics and System, Harbin Institute of Technology, Harbin 150001, China
* Correspondence: liuyubin@hit.edu.cn (Y.L.); jzhao@hit.edu.cn (J.Z.)

Abstract: Morphing aircraft can alter their aerodynamic configuration to obtain multitask adaptability and improve flight performance. In this paper, we apply the variable sweep concept on a tandem-wing micro aerial vehicle (MAV) for multitask adaptability, the two canards of which can undergo backward sweep and the two wings can undergo forward sweep. The variable sweep morphing mode can not only weaken the additional inertia forces and moments caused by morphing, but can also maintain the longitudinal dynamic balance without elevator changes, which generates trim drag. What is more, it was demonstrated that sweep morphing can exert a great effect on the aerodynamic characteristics during the transition process, which are functionalized with the sweep inputs. The effect of addition forces and moments during the transition process was analyzed by dynamic response, and the longitudinal stability of the MAV were evaluated based on a linear parameter varying (LPV) model. Due to the dramatic effects of sweep morphing on the longitudinal stability, a gain scheduled transition controller based on a convex hull algorithm is proposed to guarantee the transition stability and improve the robustness, and a linear quadratic regulator (LQR) is used to guarantee the stability of the boundary point with the consideration of input saturation. Finally, the superior performance of the proposed controller was demonstrated by a theoretical simulation based on a nonlinear model.

Keywords: variable sweep; morphing aircraft; gain scheduled; tandem-wing; mode transition; input saturation

Citation: Gao, L.; Zhu, Y.; Liu, Y.; Zhang, J.; Liu, B.; Zhao, J. Analysis and Control for the Mode Transition of Tandem-Wing Aircraft with Variable Sweep. *Aerospace* **2022**, *9*, 463. https://doi.org/10.3390/aerospace9080463

Academic Editors: David Anderson, Javaan Chahl and Michael Wing

Received: 14 July 2022
Accepted: 18 August 2022
Published: 20 August 2022

1. Introduction

The morphing concept has the capability to enhance the overall performances of aircraft [1]. One area of focus is to vary the geometry of the aircraft using an evolutionary morphing wing scheme for different flight conditions, with corresponding targets and requirements, such as a reliable cruise configuration or an efficient high-speed dash configuration [2,3]. The variable sweep wing is the first significant design for altering aircraft shape and can increase sweep angle for high-speed flight applications [4]. As a potential morphing technology to achieve multitask requirements, large-scale morphing unmanned aerial vehicles (UAVs) based either on material or shape morphing mechanisms have emerged in recent years [1]; these include shape memory alloy morphing UAV [5], various gull-wing configurations [6], span morphing UAV [7], bioinspired wing morphing [8,9], variable span and variable sweep UAV [10], etc. These UAVs are well-developed with the goal of obtaining optimal flight performance and adapting to different flight environments.

However, large-scale morphing will inevitably cause the inertia of moment, aerodynamics, and dynamics of the UAV to vary more dramatically [11], and the generated time-varying and nonlinear characteristics will cause model uncertainty, which may affect the flight quality and even threaten the flight safety, especially during the transition process [12]. Additionally, for variable sweep aircraft, sweep morphing can be considered as a

new control input; when the aircraft transforms from one state to another with the sweep morphing command, the aircraft needs to be trimmed again with an elevator for the new balanceable state [13]. Therefore, more attentions should be paid to the stability and controlling problems in the transition process of variable sweep UAV.

To evaluate the transition stability, the time-varying effects of the transition process must be considered. The gain scheduled control technique based on the LPV model has been proven to be an appropriate method for the aircraft's time-varying dynamic effects [14]. Yue et al. presented a gain self-scheduled H∞ robust control system for a tailless folding-wing morphing aircraft, which can keep the altitude and speed constant during the whole wing folding process [15]. He et al. proposed a gain scheduled control design based on a tensor product model for morphing aircraft in the transition process [16]. Moreover, a smooth switching gain scheduled controller was also applied on a variable sweep aircraft to guarantee the stability of the morphing phase [17]. In addition, the gain scheduled method allows for arbitrary morphing rates of scheduled variables to adapt to the aircraft's dynamic response, and it is able to maintain stability in various operating conditions [18–20].

In the existing literature, the additional inertia forces and moments caused by morphing are always neglected and regarded as an unmodeled term. However, the effects on the dynamics of additional inertia forces and moments are inevitable during the morphing progress, especially at the onset and end of a morphing maneuver, and the dominant forces of the additional terms are proportional to the morphing velocities and accelerations of the wing mass components [6]. Yan et al. found that a higher sweep morphing speed led to greater amplitudes of additional morphing forces and then greater amplitudes of the short-period mode parameters, and they proposed an adaptive super-twisting algorithm sliding mode controller that had good robustness for the effects of additional morphing forces [21]. Dai et al. proposed a nonlinear disturbance observer to estimate the morphing force and moment and designed a nonlinear model predictive controller considering the estimated disturbances [22]. In addition, with an appropriate morphing strategy, the additional inertia forces and moments can also be weakened, thereby relieving the burden of the control system [23].

In this paper, an innovative morphing scheme is investigated to weaken the additional inertia forces and moments caused by morphing. The morphing scheme is based on the tandem-wing MAV in our previous work [24]; the MAV has four variable sweep airfoils instead of conventional elevator and aileron, which can morph symmetrically or asymmetrically for pitch or roll control. Therefore, the shape control and flight control of the MAV are integrated, which is similar to that found in nature, inspiring us to explore appropriate morphing strategies for in-flight adaptability. Moreover, in order to satisfy multitask adaptability, the MAV needs to morph into loitering or dash configurations, which inevitably results in input saturation of the sweep morphing, which may degrade the performance of the control system or even lead to instability [25]. This also motivated us to investigate the transition control with consideration of input saturation for such a tandem-wing MAV with variable sweep. Compared with the existing results, the primary contributions of this paper are summarized as follows:

(1) An innovative variable sweep scheme integrating shape control and flight control is applied on a tandem-wing MAV for multitask requirements; the morphing scheme not only weakens the additional inertia forces and moments, but also has no trim drag generated by the traditional elevator.

(2) A gain scheduled controller with the consideration of input saturation is proposed based on the LPV model to guarantee transition process stability and satisfactory flying performance, and to improve the robustness of the considered MAV.

The remainder of this paper is outlined as follows. In Section 2, the scheme of variable sweep is presented, and the aerodynamic characteristics are systematically investigated. In Section 3, the longitudinal dynamic equations of the variable sweep MAV are linearized by the Jacobian linearization approach to achieve the LPV model, and dynamic response

and longitudinal stability are analyzed. In Section 4, a gain scheduled transition controller with the consideration of input saturation is designed based on a polytopic model to realize the required control objectives. In Section 5, numerical simulation is carried out to verify the performance of the gain scheduled transition controller. Finally, conclusions based on the presented results are presented in Section 6.

2. Variable Sweep Scheme and Aerodynamic Characteristics

2.1. Configuration of the Variable Sweep MAV

The schematic diagram and prototype of the multitask tandem-wing MAV with variable sweep are presented in Figure 1. It is a catapult launched MAV; there are four variable sweep airfoils actuated by servos with connecting rods (Figure 1a), and there is no conventional elevator or aileron. The two canards undergo backward sweep and the two wings undergo forward sweep. Using symmetric sweep morphing for pitch control, asymmetric sweep morphing for roll control can be effectively realized (Figure 1c). The MAV can change sweep angles symmetrically to reduce the wing area and wingspan for the multitask requirements. Furthermore, by allocating the sweep angles of the canards and the wings, the flight state can be trimmed without an elevator. A no-sweep configuration is used for loitering, while dashing can be realized with the large symmetric sweep configuration.

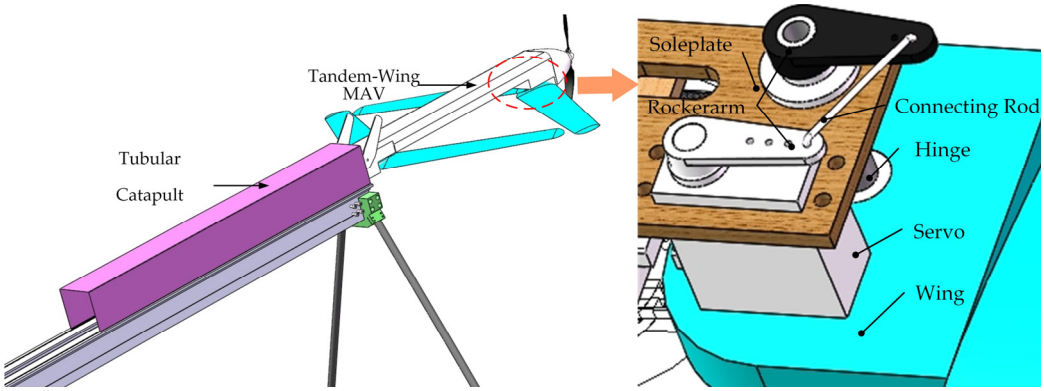

(**a**)

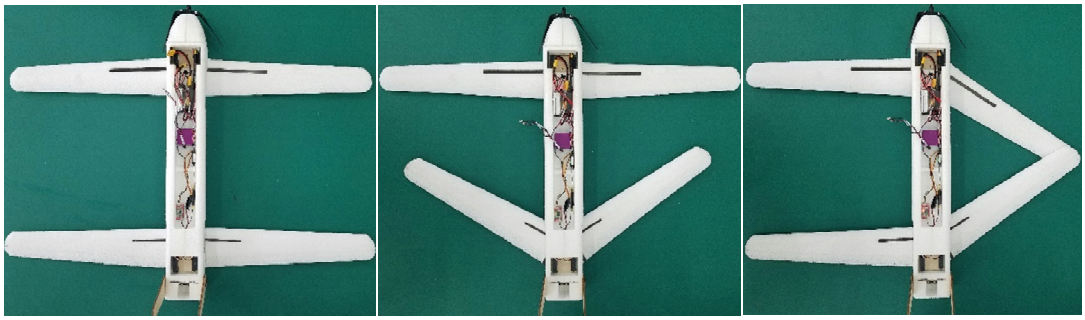

(**b**)

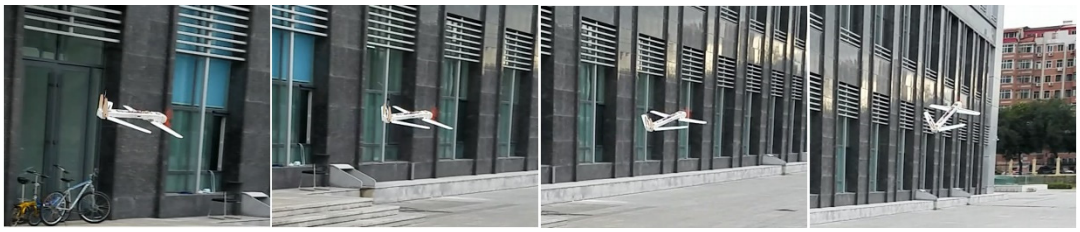

(**c**)

Figure 1. Schematic diagram and prototype of the multitask tandem-wing MAV with variable sweep. (**a**) Schematic diagram of the sweep morphing; (**b**) Prototype of the tandem-wing MAV in

different variable sweep configurations: no-sweep configuration, symmetric sweep morphing, asymmetric sweep morphing; (**c**) Flight test of symmetric morphing for pitch control.

2.2. Variable Sweep Scheme

The backward sweep angle of the canards and the forward sweep angle of the wings are defined as δ_1 and δ_2, respectively, as shown in Figure 2. When the MAV morphs from loitering configuration to dashing configuration, δ_1 and δ_2 increase according to a law that can maintain flying stability. O_b is the mass center of the fuselage, O_a is the mass center of each airfoil, l is the distance between the rotation center and the mass center of each airfoil, a_c and a_w are the distances between O_b and the rotation center of the canards and wings in the x_b axis, respectively, and b_f and c are the distances between O_b and the rotation center of the airfoils in the y_b and z_b axis, respectively. The main MAV geometric parameters and mass properties of the no-sweep configuration are shown in Table 1.

Because the oversize sweep angle will decrease the aspect ratio of the MAV significantly, thereby reducing lateral stability, δ_1 and δ_2 are limited from 0° to 30°. The morphing input saturation function can be defined as:

$$\lambda_i = \frac{\delta_i}{\delta_{\max}} = \begin{cases} 1, \delta_{i\mathrm{cmd}} > \delta_{\max} \\ \dfrac{\delta_{i\mathrm{cmd}}}{\delta_{\max}}, 0° \le \delta_{i\mathrm{cmd}} \le \delta_{\max} \\ 0, \delta_{i\mathrm{cmd}} < 0° \end{cases} \quad (1)$$

where λ_i indicates the actual variation ratio, $\delta_{i\mathrm{cmd}}$ indicates the command of sweep morphing, i = 1 and 2 denote the canards and the wings, respectively, and $\delta_{\max}$ = 30° indicates the maximum sweep angle.

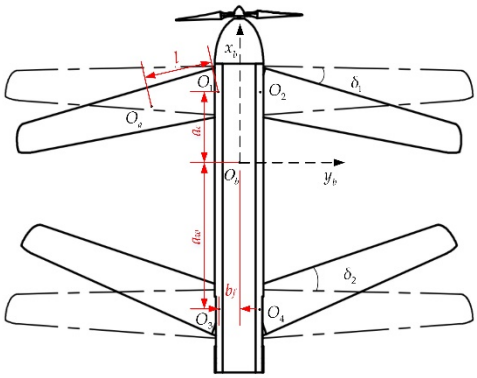

Figure 2. Definition of the sweep angles.

Table 1. Main geometric parameters of the MAV.

Parameter	Unit	Value
Length of fuselage, l_f	m	0.72
Mean aerodynamic chord, c_A	m	0.077
Span, b	m	0.89
Reference area, S	m^2	0.1345
Distance between airfoil mass center and rotation center, l	m	0.14
Distance between O_b and canard rotation center, a_c	m	0.165
Distance between O_b and wing rotation center, a_w	m	0.235
Distance in y_b axis between O_b and rotation center, b_f	m	0.04
Distance in z_b axis between O_b and rotation center, c	m	0.015
Mass of the MAV, m	kg	1.668
Mass of single airfoil, m_a	kg	0.08
Moment of inertia of fuselage, J_y^f	$kg \cdot m^2$	2.42×10^{-2}

2.3. Aerodynamic Characteristics

Variable sweep can alter the aerodynamic characteristics of the MAV significantly to realize multitask capabilities; symmetric sweep morphing mainly affects the longitudinal aerodynamics. In our study, we computed the aerodynamic forces and moments under the quasi-steady assumption. The longitudinal aerodynamic forces and moments of the MAV can be expressed by the following equation:

$$\begin{cases} L = 0.5\rho V^2 S C_L(\lambda_1, \lambda_2, \alpha) \\ D = 0.5\rho V^2 S C_D(\lambda_1, \lambda_2, \alpha) \\ M = 0.5\rho V^2 S c_A C_m(\lambda_1, \lambda_2, \alpha, q) \end{cases} \tag{2}$$

where L, D, and M are the lift, drag, and pitch moment of the MAV, respectively; C_L, C_D, and C_m are the coefficients of lift, drag, and pitch moment, respectively; α is attack angle; q is the pitch angular velocity; ρ is the air density; V is the flight velocity; S is the reference area; and c_A is the mean aerodynamic chord.

According to the quasi-steady assumption, the aerodynamic forces and moments varying with λ_1 and λ_2 are computed using the computational fluid dynamics (CFD) approach (Figure 3a); the aerodynamic derivatives are estimated by the vortex lattice method (VLM) (Figure 3b), with the same configuration. The basic non-dimensional aerodynamic coefficients of the variable sweep MAV, varying with the variation ratio and attack angle, are then fitted. The detailed expressions of aerodynamic coefficients are expressed as follows:

$$\begin{cases} C_L = \frac{1}{100}(47.95 - 4.077\lambda_1^2 - 4.579\lambda_2^2 + 16.89\lambda_1^2\lambda_2 + 17.44\lambda_1\lambda_2^2 - 20.41\lambda_1\lambda_2 - 16.23\lambda_1^2\lambda_2^2)(9.448\alpha + 0.3397) \\ C_D = \frac{1}{1000}(83.58 - 5.229\lambda_1^2 - 0.1296\lambda_2^2 - 4.34\lambda_1 - 9.409\lambda_2 + 3.595\lambda_1\lambda_2)(28.85\alpha^2 + 0.2363\alpha + 0.8429) \\ C_m = \frac{1}{100}[(-8.103 - 11.67\lambda_1^2 - 4.525\lambda_2^2 - 27.26\lambda_1 + 37.47\lambda_2)(-8.207\alpha^2 + 10.03\alpha + 0.34) \\ \quad +(7.248\lambda_1 + 36.89\lambda_2 - 69.24)q] \end{cases} \tag{3}$$

Figure 3 shows the longitudinal aerodynamic coefficients in static state, varying with λ_1 and λ_2 at $\alpha = 4°$. The lift coefficient and drag coefficient decrease gradually as λ_1 and λ_2 change from 0 to 1. The maximum of the lift coefficient and the drag coefficient are 0.4895 and 0.0836, respectively, when λ_1 and λ_2 are both equal to zero so that no morphing occurs. The minimum of the lift coefficient and the drag coefficient are 0.3698 and 0.0681, respectively, when λ_1 and λ_2 are both equal to 1, so that the MAV reaches the maximum variation ratio. The pitch moment coefficient decreases as λ_1 increases, while it increases as λ_2 increases, and the absolute value of the gradient around λ_1 is larger than that around λ_2. The main reason for this is that the effect of downwash caused by the canards would reduce the aerodynamic loads on the wings, causing the aerodynamic variation of the canards to be greater than the variation of the wings at the same variation ratio [26].

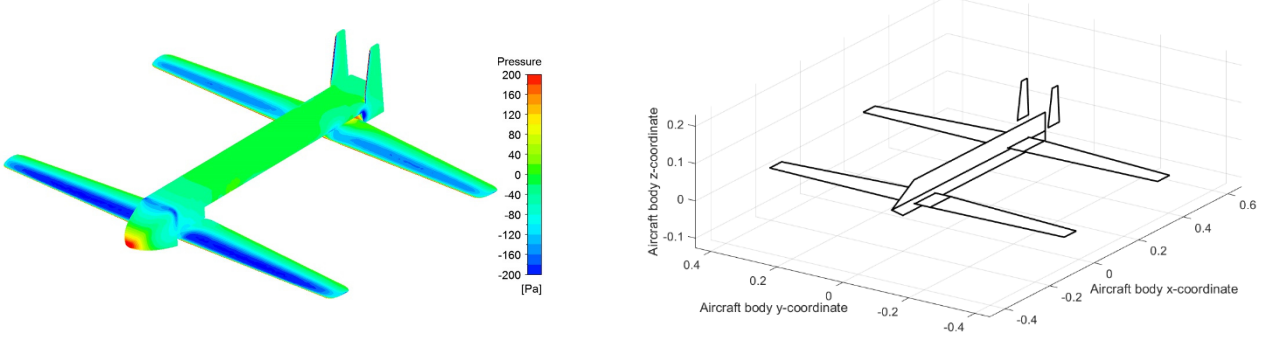

(**a**) (**b**)

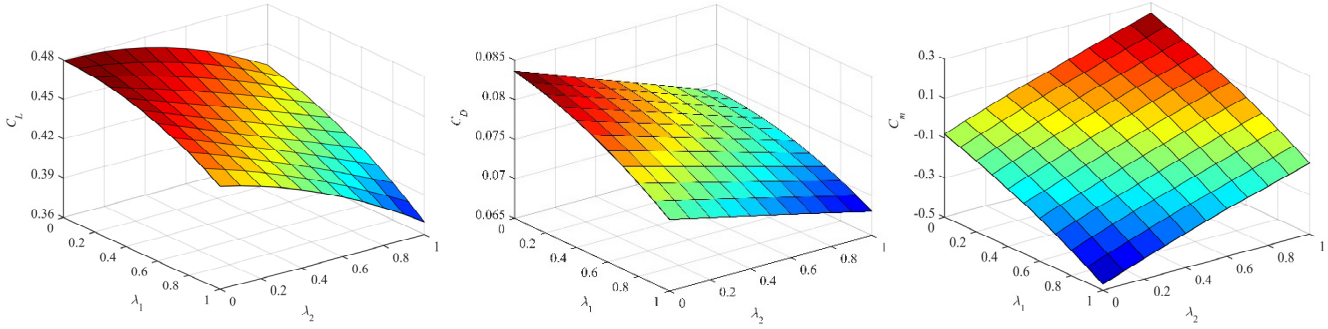

(**c**)

Figure 3. Aerodynamic characteristics acquired by CFD and VLM. (**a**) Pressure distribution on the MAV with the CFD approach; (**b**) The MAV configuration in VLM; (**c**) Aerodynamic coefficients under different variation ratios ($\alpha = 4°$): lift coefficient, drag coefficient, pitch moment coefficient.

3. Longitudinal LPV Dynamic Modeling and Stability Analysis of the Variable Sweep MAV

3.1. Longitudinal Dynamic Modeling

In the transition process of the MAV, the moment of inertia, center of gravity, and aerodynamic forces and moments have distinct changes, exhibiting clear time-varying and nonlinear characteristics. Thus, it is necessary to build an accurate and insightful dynamic model. The rigid-body dynamics method could generate many moments of inertia derivative arguments. The multi-body dynamics based on the Kane method will greatly reduce the differential operations through introducing analytical mechanics and vector mechanics [27], which would benefit the linearization of the dynamics equations. Therefore, the nonlinear dynamics equations of the MAV can be formulated based on the Kane method. Here, we only consider the longitudinal motion during the transition process of the MAV, ignoring the wind gusts and cross-flow. The longitudinal dynamic equations have been decoupled from the nonlinear multi-body dynamic model of the variable sweep MAV established in [24]. After simplification, they could be expressed as follows:

$$\begin{cases} m(\dot{u}+wq)-F_x-F_{x\delta}=0 \\ m(\dot{w}-uq)-2m_a\dot{q}(l_1-l_2)-F_z-F_{z\delta}=0 \\ J\dot{q}-2m_a(\dot{w}-uq)(l_1-l_2)+2m_ag\cos\theta(a_c-a_w)-M-M_\delta-M_{G\delta_e}=0 \\ \dot{\theta}-q=0 \end{cases} \tag{4}$$

where m is the mass of the entire MAV and m_a is the mass of a single airfoil. The mass properties of the MAV are shown in Table 1; u and w are the flight velocity in the x_b and z_b axis of the body coordinate frame, respectively, θ is the pitch angle, J represents the time-varying moment of inertia around the y_b axis, and l_1 and l_2 represent the time-varying gravity center moving of the airfoils; they are expressed as:

$$\begin{cases} J=J_y^f+4m_ac^2+4J_y^a+2m_a(l_1^{\,2}+l_2^{\,2}) \\ l_1=a_c-l\sin\delta_1 \\ l_2=a_w-l\sin\delta_2 \end{cases} \tag{5}$$

F_x and F_y are forces in the x_b and z_b axis of the body coordinate frame, respectively. According to the relationship between the body coordinate frame and the wind coordinate frame, they can be expressed as follows:

$$\begin{cases} F_x=P-mg\sin\theta-D\cos\alpha+L\sin\alpha \\ F_z=mg\cos\theta-D\sin\alpha-L\cos\alpha \end{cases} \tag{6}$$

where P is the thrust, and the thrust line passes through the origin of the body coordinate frame and is parallel to the x_b axis.

$F_{x\delta}$, $F_{z\delta}$, M_δ, and M_G are the additional inertia force in the x_b axis, the additional inertia force in the z_b axis, the additional inertia pitch moment, and the pitch moment generated by the mass center shift, respectively; they are labeled as follows:

$$\begin{cases} F_{x\delta} = 2m_a l(-\dot{\delta}_1^2 \sin\delta_1 + \dot{\delta}_2^2 \sin\delta_2 + \ddot{\delta}_1 \cos\delta_1 - \ddot{\delta}_2 \cos\delta_2) \\ F_{z\delta} = -2m_a ql(\dot{\delta}_1 \cos\delta_1 - \dot{\delta}_2 \cos\delta_2) \\ M_\delta = 2m_a cl(\ddot{\delta}_1 \cos\delta_1 + \ddot{\delta}_2 \cos\delta_2 - \dot{\delta}_1^2 \sin\delta_1 - \dot{\delta}_2^2 \sin\delta_2) + 2m_a ql(l_1\dot{\delta}_1 \cos\delta_1 + l_2\dot{\delta}_2 \cos\delta_2) \\ M_{G\delta_e} = 2m_a gl\cos\theta(\sin\delta_1 - \sin\delta_2) \end{cases} \quad (7)$$

The movements of the airfoils are parallel to the Ox_by_b plane when the MAV morphs, so transition morphing will only cause gravity center change in the x_b axis; the shift of gravity center, Δx_{cg}, is expressed as:

$$\Delta x_{cg} = \frac{2m_a l(\sin\delta_2 - \sin\delta_1)}{m} \quad (8)$$

Because δ_1 and δ_2 are limited from 0° to 30°, according to the parameters in Table 1, Δx_{cg} is not exceeding ±7 mm.

3.2. Dynamic Response Analysis during Transition Process

The open-loop dynamic responses of the transition process from loitering configuration to dashing configuration have been performed at straight and level initial flight condition at V = 20 m/s and α = 4°. The transition starts at 1 s and finishes at 3 s, as shown in Figure 4a. When the MAV morphs from the loiter configuration to the dash configuration, the canards sweep backward, and the wings sweep forward. Due to the effect of downwash on the wings, the variation ratios of the canards and the wings are different; λ_1 varies from 0 to 0.83, λ_2 varies from 0 to 1.

Figure 4b–d show variations of addition forces and moments during the transition process. It is obviously seen that the variations of the additional terms increase sharply at the onset and end of the transition, especially $F_{x\delta}$ and M_δ. In addition, according to Equation (7), the additional inertia forces and moments are relevant to the angular velocities and angular accelerations of the airfoils. Therefore, the additional terms generated by morphing all decay to zero when the transition is over. The phenomenon is similar to the results in Refs. [6,21]. However, the results in our study are quite small. The maximum of $F_{x\delta}$, $F_{z\delta}$, and M_δ are about 0.045 N, 7×10^{-5} N, and 4×10^{-3} N·m, respectively. They are considerably smaller than the aerodynamic forces and moments. This is due to the canards and wings moving towards one another during the transition process; although the variation ratios are different, the additional forces and moments generated by the canards and wings are opposite and neutralize each other, resulting in the smaller results. Moreover, the pitch moment, M_G, generated by the mass center shift still exists after transition, but the quantity is approximately 0.017 N·m, as shown in Figure 4e, and it is easy to eliminate the effect by a small amount of morphing. The shift of gravity center, Δx_{cg}, is also quite small, and the maximum is approximately 1 mm, as shown in Figure 4f. Therefore, the additional forces and moments and the changes of gravity center caused by the mode transition process for multitask capability are negligibly small, which is one of the advantages compared with conventional variable sweep aircraft.

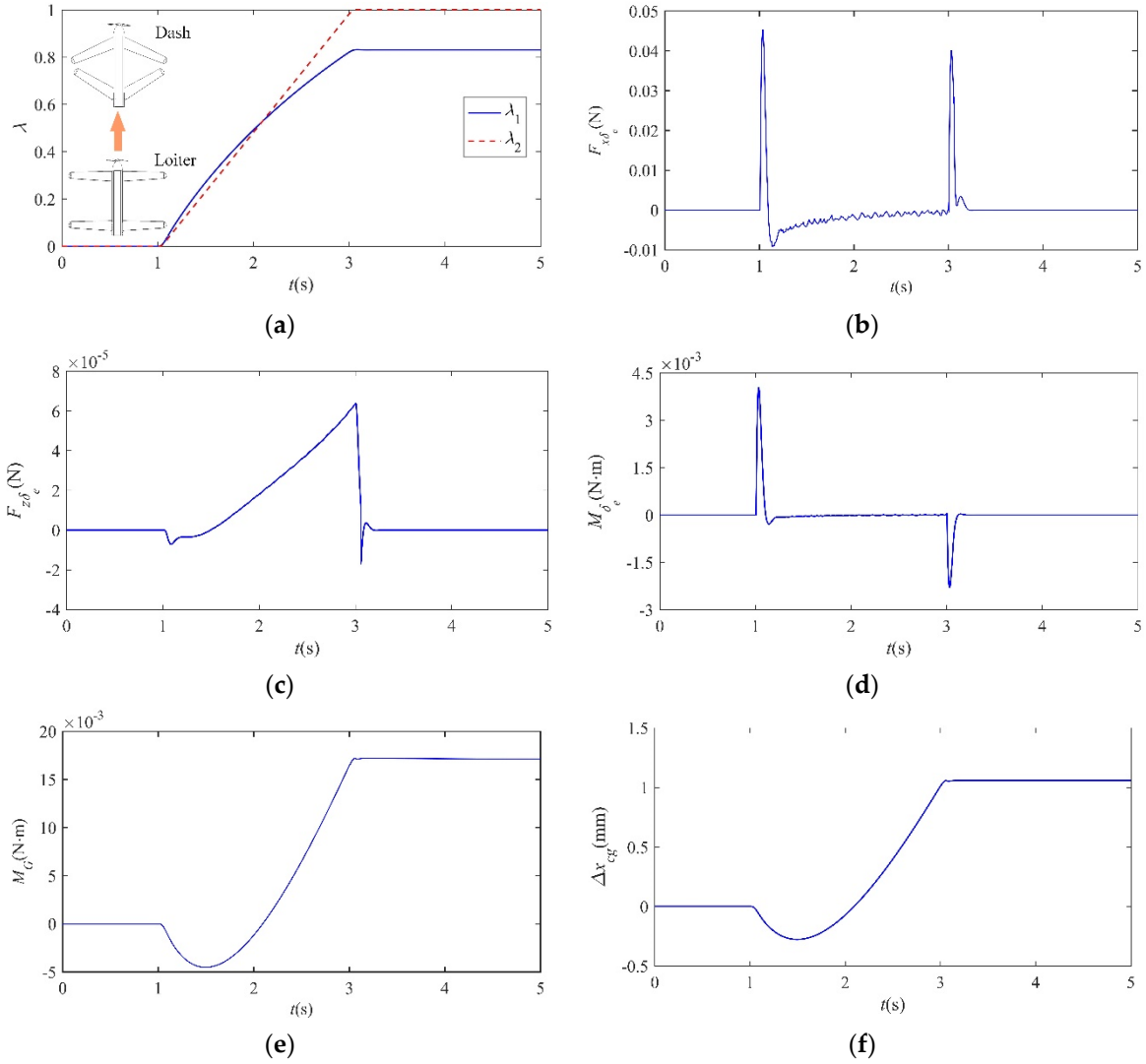

Figure 4. The open-loop dynamic responses of transition process from loitering configuration to dashing configuration. (**a**) The variation ratios during transition process; (**b**) $F_{x\delta}$, (**c**) $F_{z\delta}$, (**d**) M_{δ}, (**e**) M_G, (**f**) Shift of gravity center, Δx_{cg}.

3.3. LPV Model Establishing

According the analysis in Section 3.2, the dynamic inertial forces and moments are so small that they may have little effect on the flight control design; thus, the dynamic effects are ignored to reduce the associated complexity in the control design, but they are considered in the simulation. Instead, the controllers are required to be sufficiently robust to the dynamic effects. In order to analyze the flight state directly, the nonlinear dynamics model can be transformed in the wind coordinate frame. By combining with the height equation, the longitudinal motion equations can be represented as follows:

$$\begin{cases} -m\dot{V} + 2m_a\dot{q}(l_1 - l_2)\sin\alpha + P\cos\alpha - D + mg\sin(\alpha - \theta) = 0 \\ -mV\dot{\alpha} + mVq + 2m_a\dot{q}(l_1 - l_2)\cos\alpha - P\sin\alpha - L + mg\cos(\alpha - \theta) = 0 \\ -J\dot{q} + \dfrac{4m_a^2(l_1 - l_2)^2\dot{q}}{m} + \dfrac{2F_z m_a(l_1 - l_2)}{m} + M - 2m_a g\cos\theta(l_1 - l_2) = 0 \\ -\dot{\theta} + q = 0 \\ -\dot{h} + V\sin(\theta - \alpha) = 0 \end{cases} \tag{9}$$

where h is the height, V is the flight velocity in the wind coordinate frame, and $u = V\cos\alpha$ and $w = V\sin\alpha$.

It is difficult to design the controller directly for such a complex time-varying nonlinear system. In this paper, the Jacobian linearization approach is used to obtain the LPV model of the variable sweep MAV. By combining (2), (3), (6), and (9), the LPV model can be presented in state-space form as:

$$\bar{\boldsymbol{E}}(t)\Delta\dot{\boldsymbol{x}} = \bar{\boldsymbol{A}}(t)\Delta\boldsymbol{x} + \bar{\boldsymbol{B}}(t)\Delta\boldsymbol{u} \tag{10}$$

where $\Delta\boldsymbol{x} = [\Delta V, \Delta\alpha, \Delta q, \Delta\theta, \Delta h]^T$ and $\Delta\boldsymbol{u} = [\Delta\lambda_1, \Delta\lambda_2, \Delta\delta_T]^T$, δ_T is the thrust control and "Δ" is the deviation between the variables and their equilibrium state. $\bar{\boldsymbol{E}}(t)$, $\boldsymbol{A}(t)$, and $\boldsymbol{B}(t)$ are the time-varying configuration matrices and are given as follows:

$$\bar{\boldsymbol{E}} = \begin{bmatrix} m & 0 & -2m_a(l_1-l_2)\sin\alpha & 0 & 0 \\ 0 & mV & -2m_a(l_1-l_2)\cos\alpha & 0 & 0 \\ 0 & 0 & J-\dfrac{4m_a^2(l_1-l_2)^2}{m} & 0 & 0 \\ 0 & 0 & 0 & 1 & 0 \\ 0 & 0 & 0 & 0 & 1 \end{bmatrix} \tag{11}$$

$$\bar{\boldsymbol{A}} = \begin{bmatrix} -\dfrac{\partial D}{\partial V}+\dfrac{\partial P}{\partial V}\cos\alpha & -\dfrac{\partial D}{\partial \alpha}-P\sin\alpha+mg\cos(\alpha-\theta) & 0 & -mg\cos(\alpha-\theta) & 0 \\ -\dfrac{\partial L}{\partial V}-\dfrac{\partial P}{\partial V}\sin\alpha+mq & -\dfrac{\partial L}{\partial \alpha}-P\cos\alpha-mg\sin(\alpha-\theta) & mV & mg\sin(\alpha-\theta) & 0 \\ \dfrac{\partial M}{\partial V}+\dfrac{2m_a(l_1-l_2)}{m}\dfrac{\partial F_z}{\partial V} & \dfrac{\partial M}{\partial \alpha}+\dfrac{2m_a(l_1-l_2)}{m}\dfrac{\partial F_z}{\partial \alpha} & \dfrac{\partial M}{\partial q} & 0 & 0 \\ 0 & 0 & 1 & 0 & 0 \\ \sin(\theta-\alpha) & -V\cos(\theta-\alpha) & 0 & V\cos(\theta-\alpha) & 0 \end{bmatrix} \tag{12}$$

$$\bar{\boldsymbol{B}} = \begin{bmatrix} -\dfrac{\partial D}{\partial \lambda_1} & -\dfrac{\partial D}{\partial \lambda_2} & \dfrac{\partial P}{\partial \delta_t}\cos\alpha \\ -\dfrac{\partial L}{\partial \lambda_1} & -\dfrac{\partial L}{\partial \lambda_2} & 0 \\ \dfrac{2m_a(l_1-l_2)}{m}\dfrac{\partial F_z}{\partial \lambda_1}+\dfrac{\partial M}{\partial \lambda_1} & \dfrac{2m_a(l_1-l_2)}{m}\dfrac{\partial F_z}{\partial \lambda_2}+\dfrac{\partial M}{\partial \lambda_2} & 0 \\ 0 & 0 & 0 \\ 0 & 0 & 0 \end{bmatrix} \tag{13}$$

Because l_1 and l_2 change little with the sweep morphing, the derivatives around l_1 and l_2 are ignored in configuration matrix $\boldsymbol{B}(t)$ to reduce the complexity. For each trim condition, the new configuration matrices are computed by (11)–(13). Usually, the effects of control input on the configuration matrices are ignored in traditional aircraft, and the sweep morphing as the control input can not only affect the control moment but also the configuration matrices in our study. This aspect is the difference between a variable sweep MAV and an aircraft with traditional control surfaces.

3.4. Stability Analysis

During sweep morphing, the equilibrium states are expressed as functions of the control input. When the MAV is in level flight, the derivatives and dynamic inertial forces and moments are all zero, thus the function of the equilibrium state around the control input can be obtained from Equation (9) using the following equation:

$$\begin{cases} P - mg\sin\theta - D\cos\alpha + L\sin\alpha = 0 \\ mg\cos\theta - D\sin\alpha - L\cos\alpha = 0 \\ M - 2m_a g\cos\theta(l_1 - l_2) = 0 \\ \alpha = \theta \end{cases} \quad (14)$$

Multitask capability requires stable MAV morphing from a loitering configuration to a dashing configuration. Here, we chose several typical equilibrium states obtained using Equation (14) in loitering and dashing configurations, respectively. The corresponding trim results are summarized and presented in Table 2. Condition 1 is the initial cruising level flight state of the no-sweep configuration, corresponding to the loitering configuration where flight velocity is 20 m/s with $\alpha = 4°$. Condition 2 represents the flight state at V = 20 m/s but in dashing configuration, with the purpose of comparing the thrust with Condition 1 at the same velocity. Conditions 3 and 4 are the equilibrium states under the influence of the maximum thrust P = 5 N, with minimal and maximal variation ratio, respectively. The purpose is to compare the maximum velocity with the same thrust under the two different configurations. By comparing the trim results obtained in the loitering and dashing configurations, we can see that the sweep morphing can result in a maximal decrease by 5.72% in thrust with V = 20 m/s or a maximal increase by 9.25% in flight velocity with P = 5 N. Moreover, in each equilibrium state except the no-sweep configuration, λ_2 is larger than λ_1, which indicates that the control effectiveness of the canards is greater than that of the wings.

Table 2. Parameters of several equilibrium conditions.

Condition	1	2	3	4
λ_1	0	0.8356	0	0.8305
λ_2	0	1	0.0051	1
α (°)	4	5.481	0.806	0.926
θ (°)	4	5.481	0.806	0.926
V (m/s)	20	20	29.2	31.9
P (N)	2.761	2.603	5	5

The longitudinal mode eigenvalues of the corresponding equilibrium conditions are presented in Table 3. The negative real part of the eigenvalues demonstrate the stability of the aircraft. Remarkably, not all of the eigenvalues have negative real parts; thus, the longitudinal motion modes are not always stable under different conditions, as is the transition process between the loitering configuration and dashing configuration. In addition, the real eigenvalues represent overdamping motion, which will lead to excessive energy consumption and weak maneuver performance. Consequently, a flight control system must be applied to guarantee satisfactory flying quality and the stability of transition process.

Table 3. Eigenvalues of the corresponding equilibrium conditions.

Condition	1	2	3	4
Short-period	−8.2238 ± 2.9512 i *	−4.6568 ± 4.4176 i	−21.3151, −10.4596	−9.9703 ± 6.8222 i
Phugoid	−0.2584, 0.0901	−0.3042, 0.188	−0.2177, −0.0047	−0.1931, −0.0034

* The symbol "i" represents imaginary unit.

4. Gain Scheduled Transition Controller Synthesis with Input Saturation

According to the previous analysis, the MAV cannot remain stable all the time, especially during the transition process. Thus, the controller is designed to realize the two objectives with the consideration of input saturation:

(1) The close-loop system is asymptotic stable at the arbitrary frozen equilibrium condition.

(2) The close-loop system is affine quadratic stable during the morphing process.

4.1. Polytopic Model Conversion

If LPV systems can be converted to the polytopic model, due to the similarity between the polytope and convex hull, stability analysis and controller synthesis are only conducted for the subsystem of the vertices. The method will reduce the infinite constraints imposed on the LMIs formulation to a finite number, and it can also adjust to the variations in the plant dynamics in order to maintain stability [28]. The gain scheduled robust control based on the convex hull algorithm is used to satisfy the performance requirement along all parameter trajectories; the LQR is used to guarantee the stability of the boundary point with the consideration of input saturation.

Notations: For real symmetric matrices, $\boldsymbol{M}$, the notation $\boldsymbol{M} > 0$ stands for positive definite and indicates that all the eigenvalues of $\boldsymbol{M}$ are positive. Similarly, $\boldsymbol{M} < 0$ means negative definite, that is, all the eigenvalues of $\boldsymbol{M}$ are negative.

The LPV model of a variable sweep MAV can be transformed into the form as:

$$\begin{bmatrix} \dot{\boldsymbol{x}} \\ \boldsymbol{y} \end{bmatrix} = \begin{bmatrix} \boldsymbol{A}(\sigma) & \boldsymbol{B}(\sigma) \\ \boldsymbol{C}(\sigma) & \boldsymbol{D}(\sigma) \end{bmatrix} \begin{bmatrix} \boldsymbol{x} \\ \boldsymbol{u} \end{bmatrix} = \boldsymbol{S}(\boldsymbol{\sigma}) \begin{bmatrix} \boldsymbol{x} \\ \boldsymbol{u} \end{bmatrix} \tag{15}$$

where $\boldsymbol{A} = \overline{\boldsymbol{E}}^{-1}\overline{\boldsymbol{A}}, \boldsymbol{B} = \overline{\boldsymbol{E}}^{-1}\overline{\boldsymbol{B}}$, $\boldsymbol{y}$ is the output, $\boldsymbol{\sigma}$ is a vector of scheduling variables that consists of system outputs and inputs depended on (14), $\boldsymbol{A}(\sigma)$, $\boldsymbol{B}(\sigma)$, $\boldsymbol{C}(\sigma)$ and $\boldsymbol{D}(\sigma)$ are the continuous state-space matrices depended affinely on σ, $\sigma = (p_1, p_2, \ldots, p_n) \in \boldsymbol{\Theta}$, $p_i \in [p_{i\min}, p_{i\max}]$, and $\boldsymbol{\Theta}$ is the set of all affine parameters, $\boldsymbol{\sigma}$, and has 2^n vertices; we define the set of vertices as $\boldsymbol{\Theta}_0$.

Definition 1. *A matrix polytope is defined as the convex (Co) hull of a finite number of matrices, $\boldsymbol{T}_i$, with the same dimensions [29]:*

$$\mathrm{Co}\left\{\boldsymbol{T}_i, i = 1, 2, \cdots, k\right\} = \left\{\sum_{i=1}^{k} \rho_i \boldsymbol{T}_i : \rho_i \geq 0, \sum_{i=1}^{k} \rho_i = 1\right\} \tag{16}$$

where $\boldsymbol{\rho}_i$ represents the convex decomposition coefficient of the ith vertex of the polytopic model, which is a function of $\boldsymbol{\sigma}$.

Thus, a polytopic model can be written as:

$$\boldsymbol{S}(\boldsymbol{\sigma}) \in \mathrm{Co}\left\{\boldsymbol{S}_1, \boldsymbol{S}_2, \cdots, \boldsymbol{S}_k\right\} = \left\{\sum_{i=1}^{k} \rho_i \boldsymbol{S}_i : \rho_i \geq 0, \sum_{i=1}^{k} \rho_i = 1\right\} \tag{17}$$

where $\boldsymbol{S}_i = \begin{bmatrix} \boldsymbol{A}(\boldsymbol{\sigma}_i) & \boldsymbol{B}(\boldsymbol{\sigma}_i) \\ \boldsymbol{C}(\boldsymbol{\sigma}_i) & \boldsymbol{D}(\boldsymbol{\sigma}_i) \end{bmatrix}$ is the polytopic subsystem matrix of the ith vertex corresponding to the state vector $\boldsymbol{\sigma}_i$, $i = 1, 2, \ldots, k$, $k = 2^n$. The time-varying vector, $\boldsymbol{\sigma}$, varies within a polytope of vertices as:

$$\boldsymbol{\sigma} \in \boldsymbol{\Theta} = \mathrm{Co}\left\{\boldsymbol{\sigma}_1, \boldsymbol{\sigma}_2, \cdots, \boldsymbol{\sigma}_k\right\} = \left\{\sum_{i=1}^{k} \rho_i \boldsymbol{\sigma}_i : \rho_i \geq 0, \sum_{i=1}^{k} \rho_i = 1\right\} \tag{18}$$

and

$$\boldsymbol{\Theta}_0 = \left\{\boldsymbol{\sigma}_1, \boldsymbol{\sigma}_2, \cdots, \boldsymbol{\sigma}_k\right\}, k = 2^n \tag{19}$$

The obtained polytopic model is different according to the different weighting rules. In order to achieve a more reliable control effect, it is necessary to select appropriate weighting rules to make the polytopic model more similar to the LPV model. For the LPV model of variable sweep MAV, the configuration matrices computed by (11)–(13) mainly vary with flight velocity, V, and the angular variation ratio, λ_1 and λ_2, during the morphing process. However, λ_1 and λ_2 are not only independent morphing inputs but also flight control inputs whose relationship is dependent on (14). Considering this, we define the

scheduling parameter of the variation ratio as λ and $\lambda = \lambda_1 + \lambda_2$. According to (11)–(13), using the least squares fitting method, the LPV model can be expressed as:

$$\boldsymbol{S}(\boldsymbol{\sigma}) = \begin{bmatrix} \boldsymbol{A}_0 & \boldsymbol{B}_0 \\ \boldsymbol{C}_0 & \boldsymbol{D}_0 \end{bmatrix} + \lambda \begin{bmatrix} \boldsymbol{A}_1 & \boldsymbol{B}_1 \\ \boldsymbol{C}_1 & \boldsymbol{D}_1 \end{bmatrix} + V^2 \begin{bmatrix} \boldsymbol{A}_2 & \boldsymbol{B}_2 \\ \boldsymbol{C}_2 & \boldsymbol{D}_2 \end{bmatrix} \tag{20}$$

Therefore, the time-varying vector will be $\sigma = (\lambda, V)$, and a convex hull shown in Figure 5 will be formed with four vertices given by following:

$$\boldsymbol{\sigma}_1 = (\lambda_{\min}, V_{\min}), \boldsymbol{\sigma}_2 = (\lambda_{\max}, V_{\min}), \boldsymbol{\sigma}_3 = (\lambda_{\min}, V_{\max}), \boldsymbol{\sigma}_4 = (\lambda_{\max}, V_{\max}) \tag{21}$$

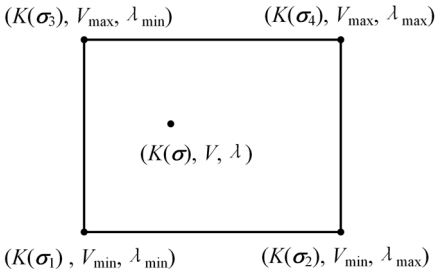

Figure 5. The rectangular convex hull decided by λ and V.

Because the LPV systems are linearly dependent on scheduling parameters, $\boldsymbol{\sigma}$, the convex decomposition coefficient can be written as follows, based on the interpolation algorithm:

$$\rho_1 = (1-x)(1-y), \rho_2 = x(1-y), \rho_3 = (1-x)y, \rho_4 = xy \tag{22}$$

$$x = \frac{\lambda - \lambda_{\min}}{\lambda_{\max} - \lambda_{\min}}, y = \frac{V^2 - V_{\min}^2}{V_{\max}^2 - V_{\min}^2} \tag{23}$$

Based on the above weighting rules, the LPV model can be approximately transformed into a polytopic model:

$$[\boldsymbol{A}(t) \quad \boldsymbol{B}(t)] \approx [\sum_{i=1}^{4} \rho_i \boldsymbol{A}(\boldsymbol{\sigma}_i) \quad \sum_{i=1}^{4} \rho_i \boldsymbol{B}(\boldsymbol{\sigma}_i)] \tag{24}$$

To evaluate the accuracy of the polytopic model, $\boldsymbol{\varepsilon}$ ($\boldsymbol{\sigma}$) is defined as the relative mismatching error between the LPV model and polytopic model [16], written as follows:

$$\boldsymbol{\varepsilon}(\boldsymbol{\sigma}) = [\boldsymbol{A}(t) \quad \boldsymbol{B}(t)] - [\sum_{i=1}^{4} \rho_i \boldsymbol{A}(\boldsymbol{\sigma}_i) \quad \sum_{i=1}^{4} \rho_i \boldsymbol{B}(\boldsymbol{\sigma}_i)] \tag{25}$$

And ε ($\boldsymbol{\sigma}$) is calculated using the matrix two-dimensional norm:

$$\varepsilon(\boldsymbol{\sigma}) = \frac{\left\| \boldsymbol{\varepsilon}(\boldsymbol{\sigma}) \right\|_2}{\left\| [\boldsymbol{A}(t) \quad \boldsymbol{B}(t)] \right\|_2} \tag{26}$$

The calculation results are shown in Figure 6. As can be seen, within the range of scheduling parameter variation, the average value of the mismatching error is about 2.9%, and the maximum value is less than 5%, which to some extent demonstrates the accuracy of the polytopic model.

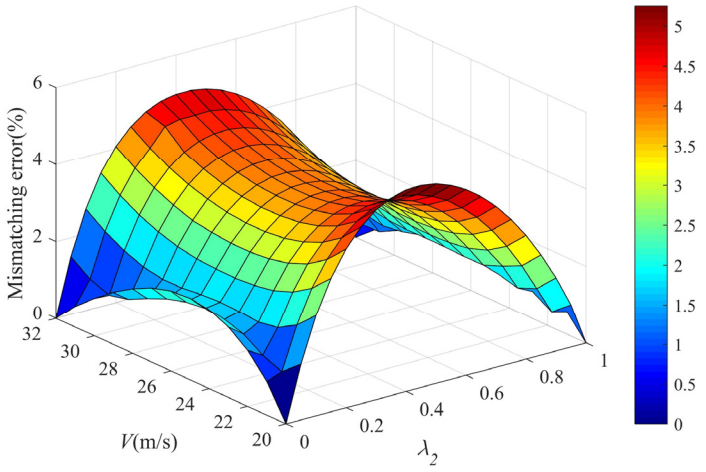

Figure 6. The mismatching error between the LPV model and the polytopic model.

4.2. Gain Scheduled Robust Control Design

Considering the polytopic model of the MAV, the gain scheduled controller is a state feedback controller in the form of the following to guarantee the affine quadratic stable of the system for all $\boldsymbol{\sigma} \in \boldsymbol{\Theta}$:

$$\boldsymbol{u} = -\boldsymbol{K}(\boldsymbol{\sigma})\boldsymbol{x} \tag{27}$$

where:

$$\boldsymbol{K}(\boldsymbol{\sigma}) \in \mathrm{Co}\left\{\boldsymbol{K}(\boldsymbol{\sigma}_1), \boldsymbol{K}(\boldsymbol{\sigma}_2), \cdots, \boldsymbol{K}(\boldsymbol{\sigma}_k)\right\} = \left\{\sum_{i=1}^{k} \rho_i \boldsymbol{K}(\boldsymbol{\sigma}_i) : \rho_i > 0, \sum_{i=1}^{k} \rho_i = 1\right\}$$

Then, the close-loop system can be transformed into the form as follows:

$$\dot{\boldsymbol{x}} = \boldsymbol{A}_c(\boldsymbol{\sigma})\boldsymbol{x} = \boldsymbol{A}(\boldsymbol{\sigma})\boldsymbol{x} - \boldsymbol{B}(\boldsymbol{\sigma})\boldsymbol{K}(\boldsymbol{\sigma})\boldsymbol{x} \tag{28}$$

According to the previous analysis of aerodynamic characteristics, the changes of aerodynamic characteristics are approximately linear with each control input. Therefore, we assume that $\boldsymbol{B}(\sigma)$ is a constant matrix as it varies in a very small range. According to this assumption, $\boldsymbol{A}_c(\sigma)$ depends affinely on σ, $\boldsymbol{\sigma} \in \boldsymbol{\Theta}$, and:

$$\boldsymbol{A}_c(\boldsymbol{\sigma}) = \sum_{i=1}^{k} \rho_i [\boldsymbol{A}(\boldsymbol{\sigma}_i) - \boldsymbol{B}\boldsymbol{K}(\boldsymbol{\sigma}_i)] = \boldsymbol{A}_{c0} + p_1\boldsymbol{A}_{c1} + p_2\boldsymbol{A}_{c2} + \cdots + p_n\boldsymbol{A}_{cn} \tag{29}$$

Theorem 1 [30]. *The sufficient condition for affine quadratic stability of the LPV system governed by (28) is the existence of n + 1 symmetric matrices* $\boldsymbol{P}_0$, $\boldsymbol{P}_1, \ldots$, $\boldsymbol{P}_n$, *for all* $\boldsymbol{\sigma} \in \boldsymbol{\Theta}_0$, *satisfying the following LMIs*:

$$\boldsymbol{A}_c^T(\boldsymbol{\sigma})\boldsymbol{P}(\boldsymbol{\sigma}) + \boldsymbol{P}(\boldsymbol{\sigma})\boldsymbol{A}_c(\boldsymbol{\sigma}) < 0 \tag{30}$$

$$\boldsymbol{P}(\boldsymbol{\sigma}) > 0 \tag{31}$$

$$\boldsymbol{A}_{ci}^T\boldsymbol{P}_i + \boldsymbol{P}_i\boldsymbol{A}_{ci} \geq 0 \tag{32}$$

where:

$$\boldsymbol{P}(\boldsymbol{\sigma}) = \boldsymbol{P}_0 + p_1\boldsymbol{P}_1 + p_2\boldsymbol{P}_2 + \cdots + p_n\boldsymbol{P}_n \tag{33}$$

When the LMIs (30)–(32) are feasible, $V(x,\boldsymbol{\sigma}) = \boldsymbol{x}^{\mathrm{T}}\boldsymbol{P}(\boldsymbol{\sigma})\boldsymbol{x}$ is a Lyapunov function of the system for all values, $\boldsymbol{\sigma} \in \boldsymbol{\Theta}$. Theorem 1 has been proven in [30]. Theorem 1 relies on the concept of multi-convexity, and the additional constraint restrictions on $\boldsymbol{P}(\sigma)$ may increase conservatism; however, the resulting criterion will always improve on the standard quadratic stability. Furthermore, Theorem 1 can be combined with a branch-and-bound scheme

to reduce conservatism through dividing the variables box into smaller hyperrectangles and reapplying Theorem 1 to each of these hyperrectangles. In our study, the scheduling variable, p_i, is assumed to be time-invariant and valued in the interval [$p_{i\min}$, $p_{i\max}$]; thus, it is easy to establish affine quadratic stability over the entire variables box [30]. The affine LPV modeling method is based on the concept of convex hulls, and the multi-convexity requirement is equivalent to the additional constraint (32); thus, constraint (32) can be satisfied for the polytope system (28). According to Theorem 1, we can summarize the corollary as follows.

Corollary 1. *Considering the polytopic model (24), if there exists, $\boldsymbol{K}(\boldsymbol{\sigma}_i)$, a positive definite matrix, $\boldsymbol{P}(\boldsymbol{\sigma}_i)$, satisfying the constraint (30) for all $\boldsymbol{\sigma}_i \in \boldsymbol{\Theta}_0$, $i = 1, 2, \ldots, 2^n$, the gain scheduled controller in the form of (27) can guarantee the affine quadratic stability of the close-loop system for all $\boldsymbol{\sigma} \in \boldsymbol{\Theta}$.*

Therefore, if the constraint (30) is satisfied for the polytopic model, the gain scheduled controller, $\boldsymbol{K}(\boldsymbol{\sigma})$, at any point inside the rectangular convex hull can be decided by (22), (23), and (37).

4.3. LQR State Feedback Control Design with Input Saturation

The LQR technique is applicable to linear time invariant (LTI) systems and has been applied in various aircraft models for stabilization augmentation and trajectory tracking [29]. A properly designed LQR controller can not only guarantee the stability of a closed loop system, but also provides optimal control performance [15]. Therefore, LQR state feedback is appropriate for the LTI system of the vertex in $\boldsymbol{\Theta}_0$. In addition, the energy consumption by large-scale sweep morphing can also be reduced with the optimal control law, which is required to minimize the performance index function, defined as:

$$J = \frac{1}{2}\int_0^\infty (\boldsymbol{x}^T\boldsymbol{Q}\boldsymbol{x} + \boldsymbol{u}^T\boldsymbol{R}\boldsymbol{u})\mathrm{d}t \tag{34}$$

where $\boldsymbol{Q}$ and $\boldsymbol{R}$ are weighting matrices and $\boldsymbol{Q} = \boldsymbol{Q}^T \geq 0$, $\boldsymbol{R} = \boldsymbol{R}^T > 0$. The corresponding full state feedback controller is given by:

$$\boldsymbol{u} = -\boldsymbol{K}(\boldsymbol{\sigma}_i)\boldsymbol{x} \tag{35}$$

Selecting appropriate $\boldsymbol{Q}$, $\boldsymbol{R}$, and solving the Riccati equation;

$$\boldsymbol{P}\boldsymbol{A} + \boldsymbol{A}^T\boldsymbol{P} - \boldsymbol{P}\boldsymbol{B}\boldsymbol{R}^{-1}\boldsymbol{B}^T\boldsymbol{P} + \boldsymbol{Q} = \boldsymbol{0} \tag{36}$$

where $\boldsymbol{P} = \boldsymbol{P}^T > 0$. The optimal control gain matrix can be obtained as:

$$\boldsymbol{K}(\boldsymbol{\sigma}_i) = \boldsymbol{R}^{-1}\boldsymbol{B}^T\boldsymbol{P} \tag{37}$$

The Lyapunov function $V(\boldsymbol{x},\boldsymbol{\sigma}_i) = \boldsymbol{x}^T\boldsymbol{P}\boldsymbol{x}$ is considered because $\boldsymbol{P}$ is a symmetric positive definite matrix, so:

$$V(\boldsymbol{x},\boldsymbol{\sigma}_i) > 0 \tag{38}$$

Combining (15) and (34)–(36), the time derivative of the function $V(\boldsymbol{x},\boldsymbol{\sigma}_i)$ can be evaluated as:

$$\begin{aligned}\dot{V}(\boldsymbol{x},\boldsymbol{\sigma}_i) &= \dot{\boldsymbol{x}}^T\boldsymbol{P}\boldsymbol{x} + \boldsymbol{x}^T\boldsymbol{P}\dot{\boldsymbol{x}} \\ &= \boldsymbol{x}^T[(\boldsymbol{A}-\boldsymbol{B}\boldsymbol{K})^T\boldsymbol{P} + \boldsymbol{P}(\boldsymbol{A}-\boldsymbol{B}\boldsymbol{K})]\boldsymbol{x} \\ &= \boldsymbol{x}^T[(\boldsymbol{A}^T - \boldsymbol{P}\boldsymbol{B}\boldsymbol{R}^{-1}\boldsymbol{B}^T)\boldsymbol{P} + \boldsymbol{P}(\boldsymbol{A}-\boldsymbol{B}\boldsymbol{R}^{-1}\boldsymbol{B}^T\boldsymbol{P})]\boldsymbol{x} \\ &= -\boldsymbol{x}^T(\boldsymbol{Q} + \boldsymbol{P}\boldsymbol{B}\boldsymbol{R}^{-1}\boldsymbol{B}^T\boldsymbol{P})\boldsymbol{x} \\ &= -\boldsymbol{x}^T\boldsymbol{Q}\boldsymbol{x} - \boldsymbol{u}^T\boldsymbol{R}\boldsymbol{u}\end{aligned} \tag{39}$$

As $\boldsymbol{Q} \geq 0$, $\boldsymbol{R} > 0$, we can assume that:

$$\dot{V}(\boldsymbol{x},\boldsymbol{\sigma}_i) \leq 0 \tag{40}$$

Obviously, if and only if $\boldsymbol{x} = \mathbf{0}$, then $\dot{V} = 0$. Thus, $\dot{V} \not\equiv 0$, and according to the Lyapunov theory, the LQR controller can guarantee the LTI model to be asymptotic and stable.

However, the inputs are restricted by the actuators; $\boldsymbol{u}_{\max}$ is defined as the maximum input and $u_{j\max}$ is the jth element of $\boldsymbol{u}_{\max}$. According to this, the system at each vertex can actually be semi-globally stabilized [31] by the state feedback law (35) for the prescribed bounded set $\boldsymbol{\Omega}_i \subset \mathbf{R}^n$; $\boldsymbol{\Omega}_i$ is contained in the domain of attraction of the equilibrium state and defined as:

$$\boldsymbol{\Omega}_i = \left\{ \boldsymbol{x} \middle| \left| k_{ij}\boldsymbol{x} \right| \le u_{j\max}, j = 1,2,3 \right\} \tag{41}$$

where k_{ij} is the jth row of the matrix $\boldsymbol{K}(\sigma_i)$.

Moreover, due to the structural restriction of the morphing MAV, the input is further restricted at the vertex condition so that the control effectiveness will reduce, thereby possibly causing the MAV to become uncontrolled. In this scenario, the closed-loop LTI model system can be rewritten as:

$$\dot{\boldsymbol{x}} = \boldsymbol{A}\boldsymbol{x} + \boldsymbol{B}\mathrm{sat}(\boldsymbol{u}) \tag{42}$$

where $\mathrm{sat}(\boldsymbol{u})$ is the control input with actuator saturation restriction.

Through the aerodynamic characteristics analysis, we can see that the aerodynamic forces vary monotonically with the control inputs λ_1 and λ_2, and the effect of λ_1 and λ_2 are opposite. Furthermore, the input saturation will only restrict the control input in one direction, thus the control torque, $\boldsymbol{B}\mathrm{sat}(\boldsymbol{u})$, is expected to satisfy:

$$\frac{1}{2}\left\| \boldsymbol{B}\boldsymbol{u} \right\| \le \left\| \boldsymbol{B}\mathrm{sat}(\boldsymbol{u}) \right\| \le \left\| \boldsymbol{B}\boldsymbol{u} \right\| \tag{43}$$

And we assume that:

$$\boldsymbol{B}\mathrm{sat}(\boldsymbol{u}) = \tau(t)\boldsymbol{B}\boldsymbol{u} \tag{44}$$

where $\tau(t)$ is a time-varying weighting coefficient and $1/2 \le \tau(t) \le 1$.

Then, the time derivative of the function $V(\boldsymbol{x},\boldsymbol{\sigma}_i)$ can be evaluated as:

$$\begin{aligned} \dot{V}(\boldsymbol{x},\boldsymbol{\sigma}_i) &= \dot{\boldsymbol{x}}^T\boldsymbol{P}\boldsymbol{x} + \boldsymbol{x}^T\boldsymbol{P}\dot{\boldsymbol{x}} \\ &= [\boldsymbol{A}\boldsymbol{x} + \boldsymbol{B}\mathrm{sat}(\boldsymbol{u})]^T\boldsymbol{P}\boldsymbol{x} + \boldsymbol{x}^T\boldsymbol{P}[\boldsymbol{A}\boldsymbol{x} + \boldsymbol{B}\mathrm{sat}(\boldsymbol{u})] \\ &= [\boldsymbol{A}\boldsymbol{x} + \tau(t)\boldsymbol{B}\boldsymbol{u}]^T\boldsymbol{P}\boldsymbol{x} + \boldsymbol{x}^T\boldsymbol{P}[\boldsymbol{A}\boldsymbol{x} + \tau(t)\boldsymbol{B}\boldsymbol{u}] \\ &= \boldsymbol{x}^T[(\boldsymbol{A}^T - \tau\boldsymbol{P}\boldsymbol{B}\boldsymbol{R}^{-1}\boldsymbol{B}^T)\boldsymbol{P} + \boldsymbol{P}(\boldsymbol{A} - \tau\boldsymbol{B}\boldsymbol{R}^{-1}\boldsymbol{B}^T\boldsymbol{P})]\boldsymbol{x} \\ &= -\boldsymbol{x}^T[\boldsymbol{Q} + (2\tau - 1)\boldsymbol{P}\boldsymbol{B}\boldsymbol{R}^{-1}\boldsymbol{B}^T\boldsymbol{P}]\boldsymbol{x} \\ &= -\boldsymbol{x}^T\boldsymbol{Q}\boldsymbol{x} - (2\tau - 1)\boldsymbol{u}^T\boldsymbol{R}\boldsymbol{u} \end{aligned} \tag{45}$$

Due to $2\tau - 1 \ge 0$, $\boldsymbol{Q} \ge 0$ and $\boldsymbol{R} > 0$, such that the LMI (40) can still hold. If and only if $\boldsymbol{x} = \mathbf{0}$, then V = 0 $\dot{V} = 0$. Thus, $\dot{V} \not\equiv 0$, and according to the Lyapunov theory, the close-loop system (42) can still be semi-globally stabilized by the state feedback law (35) when $\boldsymbol{x} \in \boldsymbol{\Omega}_i$. This implies that the controller, $\boldsymbol{K}(\sigma_i)$, designed by the LQR technique for each vertex can satisfy constraint (30). Then, according to Corollary 1, the gain scheduled controller, $\boldsymbol{K}(\sigma)$, can guarantee the affine quadratic stability of the close-loop system for the prescribed bounded set, $\boldsymbol{\Omega} \subset \mathbf{R}^n$, defined as:

$$\boldsymbol{\Omega} = \left\{ \boldsymbol{x} \middle| \left| k_j\boldsymbol{x} \right| \le u_{j\max}, j = 1,2,3 \right\} \tag{46}$$

where k_j is the jth row of the matrix, $\boldsymbol{K}(\sigma)$.

5. Simulation Results and Analysis

In order to verify the performance of the gain scheduled transition controller obtained by the method in Section 4 with the vertex flight conditions shown in Table 2, close-

loop simulations of the transition process were conducted based on the nonlinear dynamic model. The block diagram of the flight controller structure is shown in Figure 7. The observer is designed to estimate the system states. In this research, the loitering configuration corresponds to Condition 1, and the dashing configuration corresponds to Condition 4. The following two situations are considered: transition process from the loitering configuration to the dashing configuration, transition process from the dash configuration to the loiter configuration. The effect of morphing rate is also taken into account in the simulation. The airfoils are actuated by four servos housed in the fuselage. Here, we assume that the servos are described as a second order system and can provide the required moments and powers to assert the behavior [24].

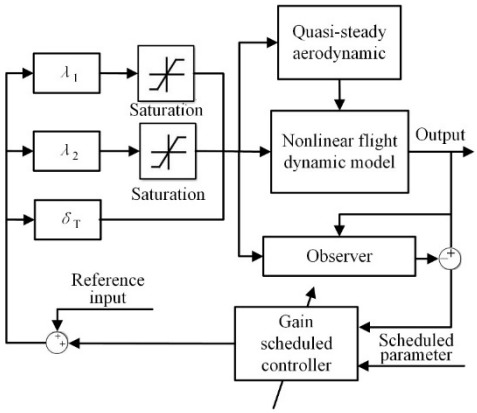

Figure 7. Control block diagram.

Figure 8 shows the close-loop dynamic responses of the transition process from loitering configuration to dashing configuration within 2 s, 5 s, and 10 s, respectively. The morphing starts with an initial flight velocity of 20 m/s at 1 s. As the morphing occurs, the flight velocity, V, increases and then converges to 31.9 m/s gradually, which corresponds to Condition 4 after the morphing finishes. Furthermore, the attack angle, α, and pitch angle, θ, are also convergent to the new equilibrium state. During the whole transition process, the variation range of altitude, h, is less than 0.1 m, and h eventually retains the initial height. In addition, it is worth noting that the close-loop system with the three different morphing rates are all stable during the transition process, and the faster morphing rate would result in a faster convergence rate as well as a larger oscillation amplitude of the state parameters. After the morphing command finishes, the sweep input, λ_2, remains almost constant due to the actuator saturation restriction, while the λ_1 and thrust, P, would continue to adjust until achieving a new balance. Moreover, λ_1 and thrust, P, both vary within acceptable ranges for the different morphing rates, which demonstrates that the gain scheduled controller can realize the transition control objective for situation 1.

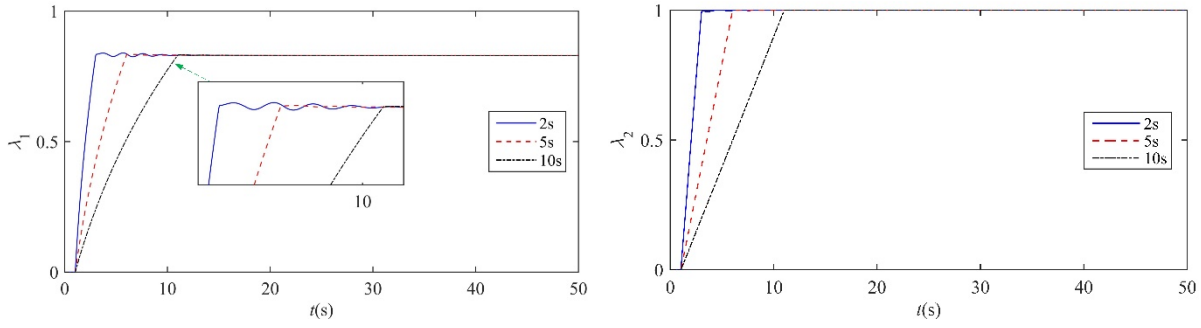

(**a**) (**b**)

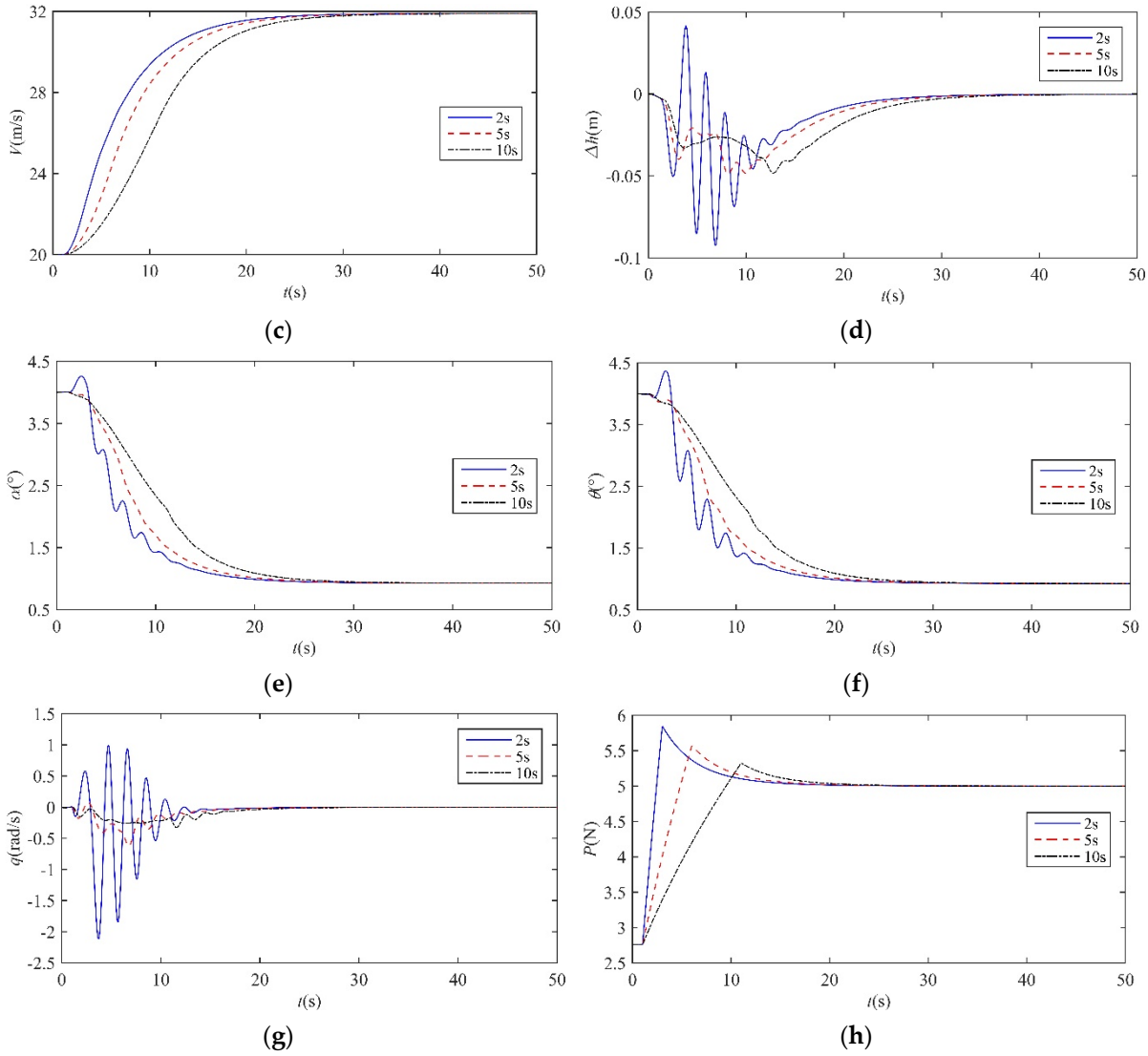

Figure 8. The dynamic responses of the transition process from loitering configuration to dashing configuration. (**a**) λ_1; (**b**) λ_2; (**c**) V; (**d**) Δh; (**e**) α; (**f**) θ; (**g**) q; (**h**) P.

Figure 9 shows the close-loop dynamic responses of the transition process from dashing configuration to loitering configuration, the corresponding flight state transforming from high speed to low speed, and the simulation was conducted with the three different morphing rates. It is observed that the transition process in situation 2 is stable. As morphing occurs, the flight velocity, V, gradually decreases from 31.9 m/s to 20 m/s, with the thrust decreasing, and all the longitudinal motion parameters finally converge to the equilibrium state of flight condition 1. Similarly, the convergence rate is faster and the oscillation amplitude of α, θ, and pitch angular velocity, q, are larger with a faster morphing rate. Furthermore, the variation range of altitude, h, is below 0.3 m and is smaller with lower morphing rates. Furthermore, q varies more placidly than that in situation 1, which demonstrates that guaranteeing the transition process stability from loitering configuration to dashing configuration faces much more challenges. Due to the placid motions, it is easy to achieve a new balanced state with only minor adjustments of the sweep control inputs. In consequence, the gain scheduled controller based on the LPV model can eliminate the disturbance caused by sweep morphing and guarantee the stability of the transition process in these two situations.

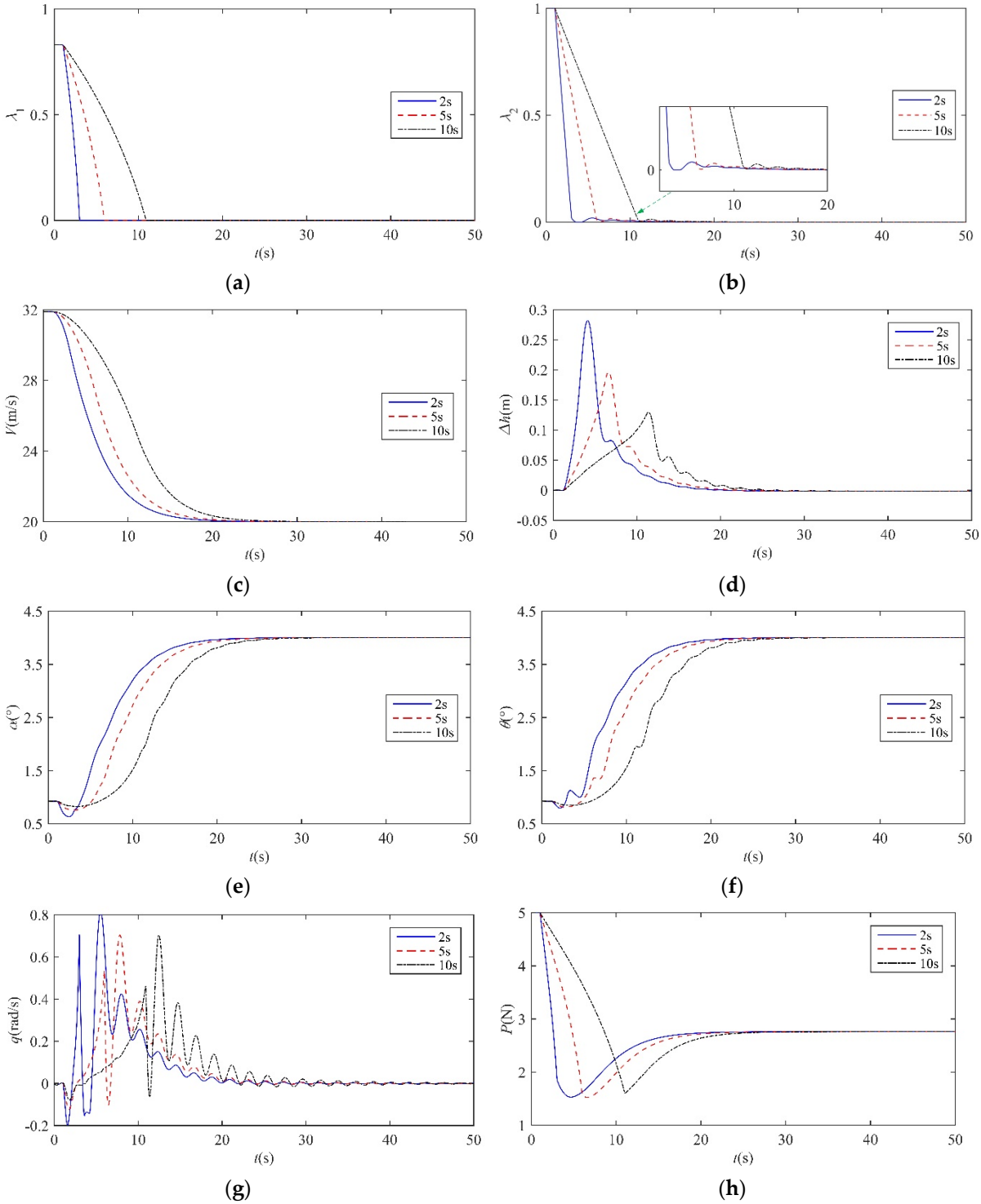

Figure 9. The dynamic responses of the transition process from dashing configuration to loitering configuration. (**a**) λ_1; (**b**) λ_2; (**c**) V; (**d**) Δh; (**e**) α; (**f**) θ; (**g**) q; (**h**) P.

As we know, unpredictable atmosphere disturbance and unmodeled dynamics exist in nearly all aircraft systems, and it is almost impossible to describe them precisely using mathematical models. Therefore, the gain scheduled controller needs to be sufficiently robust against the dynamic effects. In the following described simulations, the Gaussian white noise shown in Figure 10 is added in the pitch moment as an interference signal to verify the robustness. Figure 11 shows the close-loop dynamic responses of the transition process in the two situations under the white noise condition. The flight velocity, V, and

altitude, h, present small amplitude fluctuations under the effect of disturbance moment, while the morphing proceeds as usual without any trend of divergence. With the successive adjustments of sweep control inputs λ_1 and λ_2, the difference values of V and h between the equilibrium states are less than 0.2 m/s and 1.5 m, respectively. The simulation results demonstrate that the designed gain scheduled transition controller has strong robustness for random disturbance.

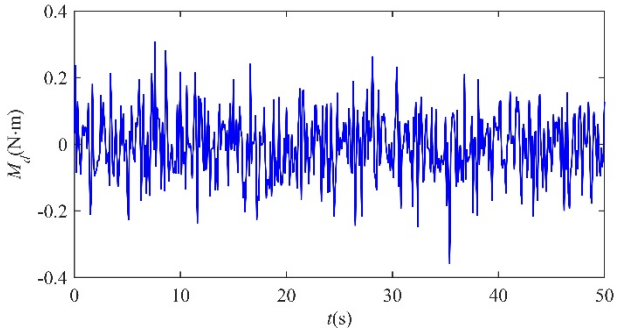

Figure 10. The Gaussian white noise disturbance moment.

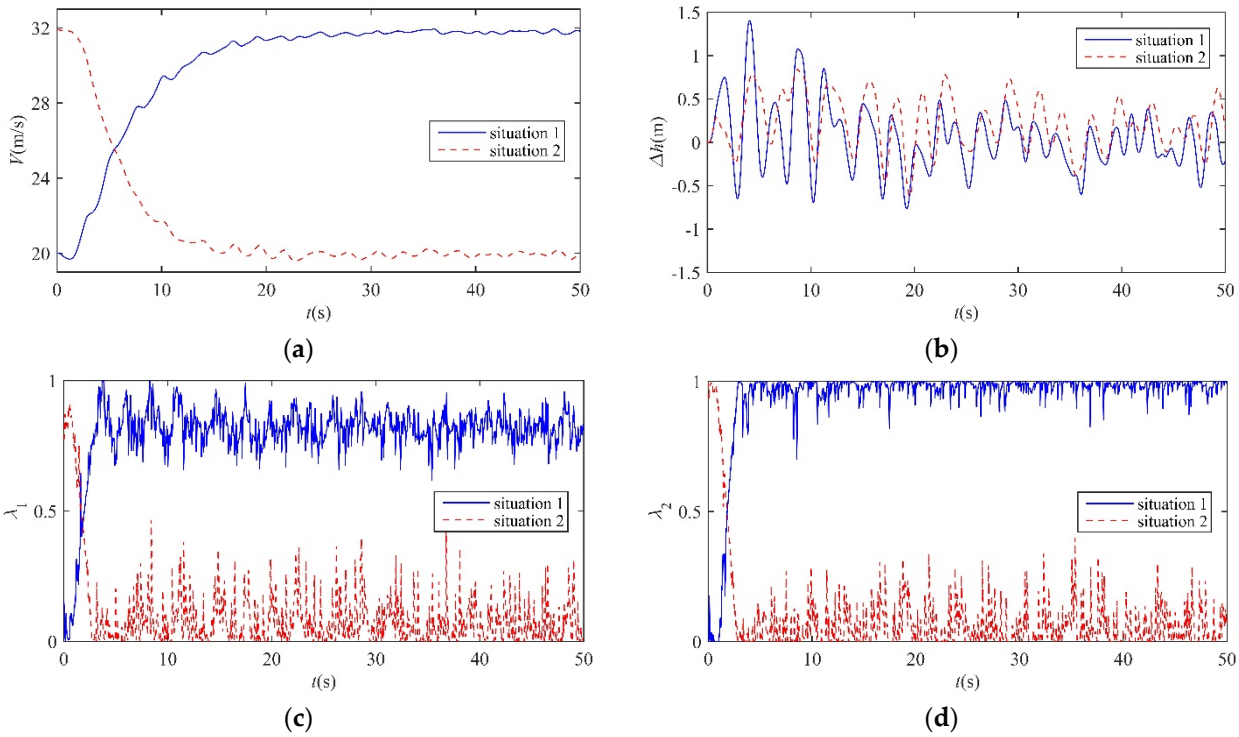

Figure 11. The dynamic responses of the transition process under white noise condition. (**a**) V; (**b**) Δh; (**c**) λ_1; (**d**) λ_2.

6. Conclusions

In this paper, an innovative variable sweep scheme was applied to a tandem-wing MAV of which the shape control and flight control are integrated, and multitask adaptability could be achieved by symmetric sweep morphing to alter the configuration of the considered MAV without elevator changes. For the large-scale morphing MAV, the aerodynamic effects caused by sweep morphing were presented through a numerical simulation method and functionalized with the sweep inputs. A nonlinear longitudinal dynamic model for the considered MAV was then proposed, and the additional terms generated by morphing were decomposed and simulated by open-loop dynamic response. The results showed that the additional forces and moments and the changes of gravity center

caused by the mode transition process were negligibly small. The LPV model was obtained by the Jacobian linearization approach to approximately characterize the complex behavior of the transition process. The stability analysis based on the LPV model showed that the MAV was not always stable under different equilibrium conditions, as well as during the transition process. Furthermore, the LPV model was converted to a polytopic model, and the average value of mismatching error between the LPV model and the polytopic model was about 2.9%. Based on the polytopic model, a gain scheduled controller was proposed to guarantee the affine quadratic stability of the close-loop model during the morphing process, and the LQR method was used to guarantee asymptotic stability and improve the robustness at the arbitrary frozen equilibrium condition. Furthermore, the Lyapunov function proved that the controller could still satisfy the asymptotic stability with the consideration of input saturation. Finally, the results of simulation based on the nonlinear model demonstrated that the proposed controller exhibits great performance during the transition process between the loitering configuration and dash configuration. In addition, the simulation under the effect of disturbance moment illustrated that the designed gain scheduled transition controller had strong robustness against random white noise.

In our future works, we will pay attention to adaptive sliding mode control for attitude control; the morphing MAV's dynamic model representation will be further optimized to improve control precision, and flight tests will also be carried out.

Author Contributions: Conceptualization, L.G.; formal analysis, L.G.; funding acquisition, J.Z. (Jie Zhao); investigation, Y.Z. and Y.L.; methodology, L.G. and Y.Z.; supervision, Y.Z. and J.Z. (Jie Zhao); validation, J.Z. (Junming Zhang) and B.L.; writing—original draft, L.G.; writing—review and editing, Y.L. All authors have read and agreed to the published version of the manuscript.

Funding: This research was funded by the China Postdoctoral Science Foundation, grant number 2021M690831 and Self-Planned Task of State Key Laboratory of Robotics and System (HIT), grant number No. SKLRS202103C.

Institutional Review Board Statement: Not applicable.

Informed Consent Statement: Not applicable.

Data Availability Statement: Not applicable.

Conflicts of Interest: The authors declare no conflict of interest.

Abbreviations

λ_1	variation ratio of canard	F_y	forces in z_b axis
λ_2	variation ratio of wing	P	thrust
δ_{1cmd}	command of canard morphing	$F_{x\delta}$	additional inertia force in x_b axis
δ_{2cmd}	command of wing morphing	$F_{z\delta}$	additional inertia force in z_b axis
L	lift	M_δ	additional inertia pitch moment
D	drag	M_G	pitch moment generated by the mass center shift
M	pitch moment	Δx_{cg}	shift of gravity center
C_L	lift coefficient	h	height
C_D	drag coefficient	δ_T	hrust control
C_m	pitch moment coefficient	"Δ"	deviation between the variables and equilibrium state
α	attack angle	ρ_i	convex decomposition coefficient
q	pitch angular velocity	$\boldsymbol{\sigma}$	vector of scheduling variables
ρ	air density	$\boldsymbol{\Theta}$	set of all affine parameter
V	flight velocity	$\boldsymbol{\Theta}_0$	set of vertices
u	flight velocity in x_b axis	$\boldsymbol{\varepsilon}(\boldsymbol{\sigma})$	relative mismatching error

w	flight velocity in z_b axis	$\boldsymbol{Q}$	weighting matrix
θ	pitch angle	$\boldsymbol{R}$	weighting matrix
J	time-varying moment of inertia	$\boldsymbol{K}(\sigma)$	gain scheduled controller
F_x	forces in x_b axis	sat($\boldsymbol{u}$)	control input with actuator saturation restriction

References

1. Li, D.; Zhao, S.; Da Ronch, A.; Xiang, J.; Drofelink, J.; Li, Y.; Zhang, L.; Wu, Y.; Kintscher, M.; Monner, H.P.; et al. A review of modelling and analysis of morphing wings. *Prog. Aerosp. Sci.* **2018**, *100*, 46–62.
2. Dai, P.; Yan, B.; Huang, W.; Zhen, Y.; Wang, M.; Liu, S. Design and aerodynamic performance analysis of a variable-sweep-wing morphing waverider. *Aerosp. Sci. Technol.* **2020**, *98*, 105703.
3. Chang, E.; Matloff, L.Y.; Stowers, A.K.; Lentink, D. Soft biohybrid morphing wings with feathers underactuated by wrist and finger motion. *Sci. Robot.* **2020**, *5*, eaay1246.
4. Kress, R. Variable sweep wing designs. In *Aircraft Prototype & Technology Demonstrator Symposium*; Aerospace Research Central: Dayton, OH, USA, 1983; pp. 43–61.
5. Han, M.W.; Rodrigue, H.; Kim, H.I.; Song, S.H.; Ahn, S.H. Shape memory alloy/glass fiber woven composite for soft morphing winglets of unmanned aerial vehicles. *Compos. Struct.* **2016**, *140*, 202–212.
6. Obradovic, B.; Subbarao, K. Modeling of flight dynamics of morphing-wing aircraft. *J. Aircr.* **2011**, *48*, 391–402.
7. Ajaj, R.; Jankee, G. The transformer aircraft: A multimission unmanned aerial vehicle capable of symmetric and asymmetric span morphing. *Aerosp. Sci. Technol.* **2018**, *76*, 512–522.
8. Sui, T.; Zou, T.; Riskin, D. Optimum design of a novel bio-inspired bat robot. *IEEE Robot. Autom. Lett.* **2022**, *7*, 3419–3426.
9. Ajanic, E.; Feroskhan, M.; Mintchev, S.; Noca, F.; Floreano, D. Bioinspired wing and tail morphing extends drone flight capabilities. *Sci. Robot.* **2020**, *5*, eabc2897.
10. Mir, I.; Maqsood, A.; Eisa, S.A.; Taha, H.; Akhtar, S. Optimal morphing–augmented dynamic soaring maneuvers for unmanned air vehicle capable of span and sweep morphologies. *Aerosp. Sci. Technol.* **2018**, *79*, 17–36.
11. Shi, R.; Wan, W. Analysis of flight dynamics for large-scale morphing aircraft. *Aircr. Eng. Aerosp. Technol.* **2015**, *87*, 38–44.
12. Chakravarthy, A.; Grant, D.; Lind, R. Time-varying dynamics of a micro air vehicle with variable-sweep morphing. *J. Guid. Control Dyn.* **2012**, *35*, 890–903.
13. Cheng, H.; Shi, Q.; Wang, H.; Shan, W.; Zeng, T. Flight dynamics modeling and stability analysis of a tube-launched tandem wing aerial vehicle during the deploying process. *Proc. Inst. Mech. Eng. Part G J. Aerosp. Eng.* **2021**, *236*, 262–280.
14. Seigler, T.M.; Neal, D.A. Analysis of transition stability for morphing aircraft. *J. Guid. Control Dyn.* **2012**, *32*, 1947–1954.
15. Yue, T.; Wang, L.; Ai, J. Gain self-scheduled H∞ control for morphing aircraft in the wing transition process based on an LPV model. *Chin. J. Aeronaut.* **2013**, *26*, 909–917.
16. He, Z.; Yin, M.; Lu, Y. Tensor product model-based control of morphing aircraft in transition process. *Proc. Inst. Mech. Eng. Part G J. Aerosp. Eng.* **2016**, *230*, 378–391.
17. Jiang, W.; Dong, C.; Wang, Q. A systematic method of smooth switching LPV controllers design for a morphing aircraft. *Chin. J. Aeronaut.* **2015**, *28*, 1640–1649.
18. Fan, W.; Liu, H.H.T.; Kwong, R.H.S. Gain-Scheduling Control of Flexible Aircraft with Actuator Saturation and Stuck Faults. *J. Guid. Control Dyn.* **2017**, *40*, 510–520.
19. Jiang, W.; Wu, K.; Wang, Z.; Wang, Y. Gain-scheduled control for morphing aircraft via switching polytopic linear parameter-varying systems. *Aerosp. Sci. Technol.* **2020**, *107*, 106242.
20. Poksawat, P.; Wang, L.; Mohamed, A. Gain scheduled attitude control of fixed-wing UAV with automatic controller tuning. *Aerosp. Sci. Technol.* **2018**, *26*, 1192–1203.
21. Yan, B.; Dai, P.; Liu, R.; Xing, M.; Liu, S. Adaptive super-twisting sliding mode control of variable sweep morphing aircraft. *Aerosp. Sci. Technol.* **2019**, *92*, 198–210.
22. Dai, P.; Liu, R.; Liu, S.; Wang, M. Modeling and Nonlinear Model Predictive Control of a Variable-sweep-wing Morphing Waverider. *IEEE Access* **2021**, *9*, 63510–63520.
23. Yang, G.T.; Tang, S.J.; Zhao, L.D.; Guo, J. Dynamic modeling and response of a morphing uav with variable sweep and variable span. *Binggong Xuebao Acta Armamentarii* **2014**, *35*, 102–107.
24. Gao, L.; Jin, H.; Zhao, J.; Cai, H.; Zhu, H. Flight dynamics modeling and control of a novel catapult launched tandem-wing micro aerial vehicle with variable sweep. *IEEE Access* **2018**, *6*, 42294–42308.
25. Wu, Z.; Lu, J.; Zhou, Q. Modified adaptive neural dynamic surface control for morphing aircraft with input and output constraints. *Nonlinear Dyn.* **2017**, *87*, 2367–2383.
26. Gao, L.; Li, C.; Jin, H.; Zhu, H.; Zhao, J.; Cai, H. Aerodynamic characteristics of a novel catapult launched morphing tandem-wing unmanned aerial vehicle. *Adv. Mech. Eng.* **2017**, *9*, 1–15.
27. Zhang, X.; Huang, Y.; Chen, X.; Han, W. Modeling of a space flexible probe-cone docking system based on the Kane method. *Chin. J. Aeronaut.* **2014**, *27*, 248–258.
28. Kumar, A.; Andersen, M.R. A comparison of LPV modeling techniques for aircraft control. In AIAA Guidance, Navigation and Control Conference and Exhibit, Denver, CO, USA, 14–17 August 2000; p. 4458.

29. Baldelli, D.H.; Lee, D.H.; Pena, R.S.S.; Cannon, B. Modeling and control of an aeroelastic morphing vehicle. *J. Guid. Control Dyn.* **2008**, *31*, 1687–1699.
30. Gahinet, P.; Apkarian, P.; Chilali, M. Affine parameter-dependent Lyapunov functions and real parametric uncertainty. *IEEE Trans. Autom. Control* **1996**, *41*, 436–442.
31. Lin, Z.; Saberi, A. A semi-global low-and-high gain design technique for linear systems with input saturation–stabilization and disturbance rejection. *Int. J. Robust Nonlinear Control* **1995**, *5*, 381–398.